Role of hydrogen in high-yield growth of boron nitride nanotubes at atmospheric pressure by induction thermal plasma

Kim, Keun Su; Couillard, Martin; Shin, Homin; Plunkett, Mark; Ruth, Dean; Kingston, Christopher T.; Simard, Benoit

Publisher's version / Version de l'éditeur:
https://doi.org/10.1021/acsnano.7b08708
ACS Nano, 12, 1, pp. 884-893, 2018-01-04

ACS NANO
Cite This: ACS Nano 2018, 12, 884−893
www.acsnano.org

ARTICLE

Role of Hydrogen in High-Yield Growth of Boron Nitride Nanotubes at Atmospheric Pressure by Induction Thermal Plasma

Keun Su Kim,*[,†,§] Martin Couillard,[‡] Homin Shin,[†] Mark Plunkett,[†] Dean Ruth,[†] Christopher T. Kingston,[†] and Benoit Simard*[,†]

[†]Security and Disruptive Technologies Research Centre, Emerging Technologies Division, National Research Council Canada, Ottawa, Ontario K1A 0R6, Canada

[‡]Energy, Mining and Environment Research Centre, Engineering Division, National Research Council Canada, Ottawa, Ontario K1A 0R6, Canada

[§]Department of Mechanical and Industrial Engineering, University of Toronto, 5 King's College Road, Toronto, Ontario M5S 3G8, Canada

Supporting Information

ABSTRACT: We recently demonstrated scalable manufacturing of boron nitride nanotubes (BNNTs) directly from hexagonal BN (hBN) powder by using induction thermal plasma, with a high-yield rate approaching 20 g/h. The main finding was that the presence of hydrogen is crucial for the high-yield growth of BNNTs. Here we investigate the detailed role of hydrogen by numerical modeling and *in situ* optical emission spectroscopy (OES) and reveal that both the thermofluidic fields and chemical pathways are significantly altered by hydrogen in favor of rapid growth of BNNTs. The numerical simulation indicated improved particle heating and quenching rates (~10^5 K/s) due to the high thermal conductivity of hydrogen over the temperature range of 3500−4000 K. These are crucial for the complete vaporization of the hBN feedstock and rapid formation of nanosized B droplets for the subsequent BNNT growth. Hydrogen is also found to extend the active BNNT growth zone toward the reactor downstream, maintaining the gas temperature above the B solidification limit (~2300 K) by releasing the recombination heat of H atoms, which starts at 3800 K. The OES study revealed that H radicals also stabilize B or N radicals from dissociation of the feedstock as BH and NH radicals while suppressing the formation of N_2 or N_2^+ species. Our density functional theory calculations showed that such radicals can provide faster chemical pathways for the formation of BN compared with relatively inert N_2.

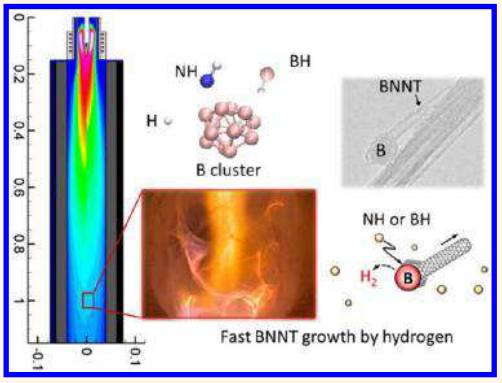

KEYWORDS: *boron nitride nanotubes, scalable manufacturing, hydrogen-catalyzed, induction thermal plasma, thermofluid simulation, optical emission spectroscopy, density functional theory*

Discovering effective growth enhancers of various nanomaterials and unraveling their detailed roles are critical steps in nanoscience and nanotechnology research. Water-assisted carbon nanotube (CNT) synthesis is a well-known example of such developments that has greatly advanced the CNT research field.[1] Boron nitride nanotubes (BNNTs) are structural analogues of CNTs composed of single- or few-layer hexagonal BN (hBN) sheets.[2] These one-dimensional nanomaterials also represent an immense potential in science and technology featuring a set of unique properties distinguished from CNTs.[3−5] Since the first synthesis in 1995,[6] their scalable manufacturing has been of particular interest, exploring different synthesis techniques and seeking effective growth enhancers.[7−10] Although some methods have already demonstrated gram-quantity production, unlike the CNT case, it is still challenging to produce BNNTs at large scales, particularly those with few walls (<3) and small diameters (<5 nm).[11]

Among various BNNT synthesis techniques, the high-temperature routes by lasers[12,13] or thermal plasmas[14,15] have demonstrated great potential for the large-scale synthesis of highly crystalline, small-diameter BNNTs directly from pure B or BN sources. In those approaches, B-containing feedstocks

Received: December 8, 2017
Accepted: January 4, 2018
Published: January 4, 2018

are vaporized at high temperatures above 3000 K to form nanosized B droplets. BNNTs grow continuously from those B droplets by incorporation of N-containing species such as N_2. Despite their good scalability, the major challenge has been the relatively slow reaction between B droplets and N_2 (*i.e.*, $2B + N_2 \rightarrow 2BN$) at atmospheric pressure, due to the strong triple bond of N_2 with a high bond dissociation energy (BDE) of 945 kJ/mol.[16] Recently there has been notable progress in addressing this particular issue.[11] High-pressure environments (*e.g.*, 0.2−2 MPa) are found to be highly effective in driving the reaction toward BN formation;[17,18] however, it would be more favorable in terms of scalability if one could produce similar-quality BNNTs at atmospheric pressure.

In 2014 we reported a very efficient route for the synthesis of BNNTs at atmospheric pressure using a high-temperature plasma process (Figure 1).[19] This new plasma process made use of hydrogen as a growth enhancer, which dramatically increased the yield of small-diameter BNNTs (*i.e.*, ~20 g/h, <5 nm) even at atmospheric pressure. In the absence of hydrogen, however, the products were largely amorphous B particles, attesting to the inefficiency of the direct reaction of B and N_2. In our previous paper,[19] we speculated that the presence of hydrogen might have facilitated the formation of B−N−H-containing species (*e.g.*, BH_3NH_3, $H_6B_3N_3$) *in situ*. Compared with N_2, such compounds can provide faster chemical pathways for BN formation because of their relatively low BDEs; however, our previous hypothesis was largely based on indirect observation from the reaction byproducts extracted, which are not even stable in the temperature range suitable for BNNT growth (~3000 K). We still lack convincing evidence that can clearly elucidate the role of hydrogen.

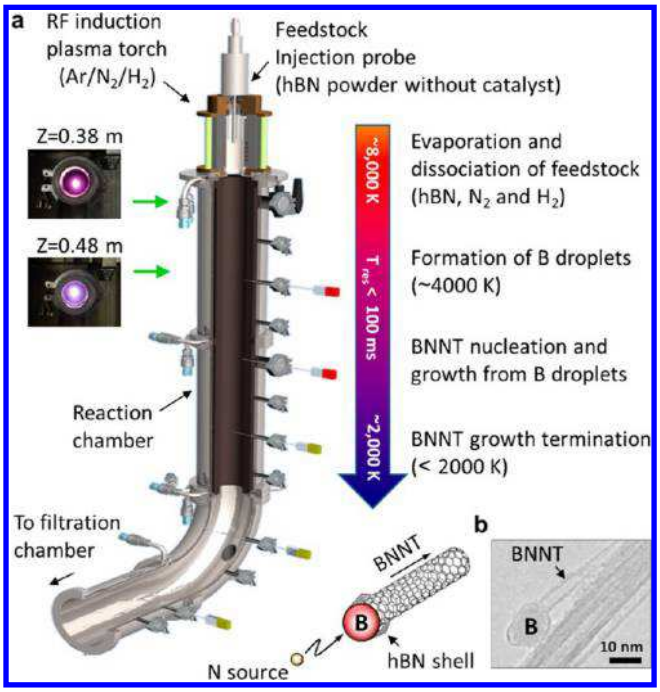

Figure 1. Hydrogen-assisted boron nitride nanotube synthesis (HABS) process.[19] (a) Schematic of the HABS process developed for the large-scale synthesis of BNNTs. (b) High-magnification TEM image of a BNNT suggesting the vapor−liquid−solid (VLS) growth mechanism.[20]

Here we investigate the detailed role of hydrogen in the hydrogen-assisted BNNT synthesis (HABS)[19] using both thermofluid simulation and *in situ* optical emission spectroscopy (OES). In the HABS process, the BNNT synthesis is accomplished *via* both physical and chemical processes. The physical processes include evaporation and condensation, in which the hBN feedstock is first heated and vaporized and then those vapors are subsequently subjected to rapid quenching to form B droplets through homogeneous nucleation. The formed B droplets are assumed to serve as nucleation sites for BNNTs (Figure 1b).[20] The chemical process involves chemical reactions leading to the formation of gaseous BNNT precursors at the early stage of the process and their subsequent reactions with B droplets for BNNT growth. In this work, the effect of hydrogen on the physical processes such as feedstock vaporization and nucleation of B droplets was studied using thermofluid simulation, whereas the hydrogen-mediated plasma chemistry was investigated *in situ* using OES. Our study revealed that both the physical and chemical processes are significantly altered by the presence of hydrogen in favor of rapid growth of BNNTs.

RESULTS AND DISCUSSION

Effects of Hydrogen in BNNT Synthesis. To investigate the effects of hydrogen, three synthesis experiments were carried out with different H_2 contents in the plasma gas: 0 vol %, 12 vol %, and 24 vol %. In each case, hBN powder (99.5%, avg. 70 nm, MK-hBN-N70, M K Impex Corp.) was employed as the feedstock without a metal catalyst. The following operating conditions were used for plasma generation: powder carrier gas (Ar) at 3 L/min; central gas (Ar) at 30 L/min; sheath gas ($Ar/N_2/H_2$) at 55/135/0 (0% H_2), 55/135/30 (12% H_2) or 25/135/60 (24% H_2) L/min; 45 kW plate power at 93 kPa. The detailed synthesis protocol can be found elsewhere.[19]

Figure 2a shows photographs of the materials formed inside the reaction chamber in the presence of hydrogen after 0, 10, 15, and 20 min. Within 10 min BNNT strands were observed and rapidly entangled to form BNNT webs. The BNNT webs continuously incorporated freshly formed BNNTs from the reaction stream and eventually turned into nonwoven BNNT membranes. After 20 min the plasma jet became almost invisible as more materials built up. After operation for 4 h, the reactor was full of material, as shown in Figure 2b, and the demonstrated production rate approached 20 g/h; however, in the absence of hydrogen, the reactor inner walls were merely coated with dark, powdery material (*i.e.*, elemental B) without any signs of web or membrane formation (not shown).

The effect of hydrogen on the morphological properties of the reaction products was investigated using scanning electron microscopy (SEM) and transmission electron microscopy (TEM). Figure 3a−c shows images of the as-produced sample obtained using 24 vol % H_2; densely entangled fibrous materials are primarily observed, with some particulate impurities. The TEM image (Figure 3c) confirms that those fibrous materials have tubular structures with small diameters (avg. 5 nm) without severe structural defects (inset of Figure 3c). Further elemental analysis by electron energy loss spectroscopy (EELS) confirmed that abundant high-quality BNNTs were synthesized in the presence of hydrogen.[19] Upon reduction of the hydrogen content in the plasma gas to 12 vol %, the BNNT content in the sample decreased, and more nontubular impurities were generated (Figure S1a). In addition, the extremities of the BNNTs became more visible, implying that shorter BNNTs were produced in this case (Figure S1b). Figure 3d−f shows images of the sample produced with 0 vol % H_2. The SEM and

DOI: 10.1021/acsnano.7b08708
ACS Nano 2018, 12, 884−893

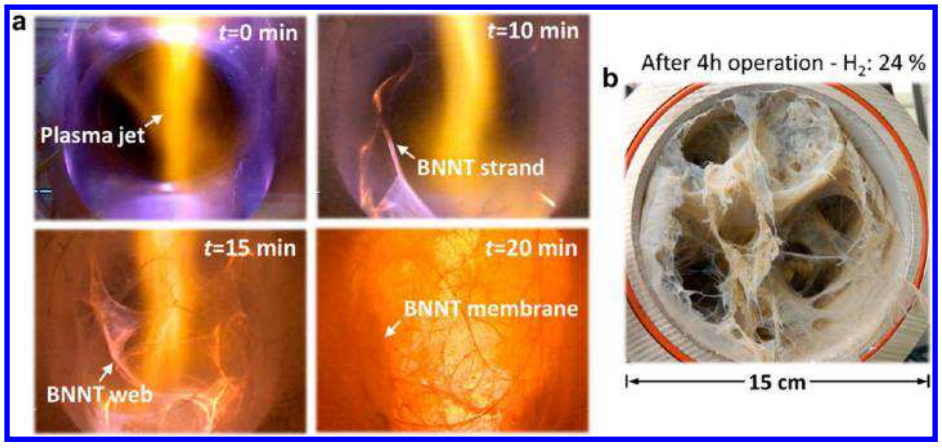

Figure 2. Growth of BNNTs in the HABS process. (a) Photographs of the reaction product formed inside the reactor after 0, 10, 15, and 20 min. (b) Photograph of the reaction product after operation for 4 h. Synthesis conditions: hBN powder (avg. 70 nm) at 0.5−1.0 g/min; carrier gas (Ar) at 3 L/min; central gas (Ar) at 30 L/min, sheath gas ($Ar/N_2/H_2$) at 25/135/60 L/min; plate power of 45 kW at 93 kPa.

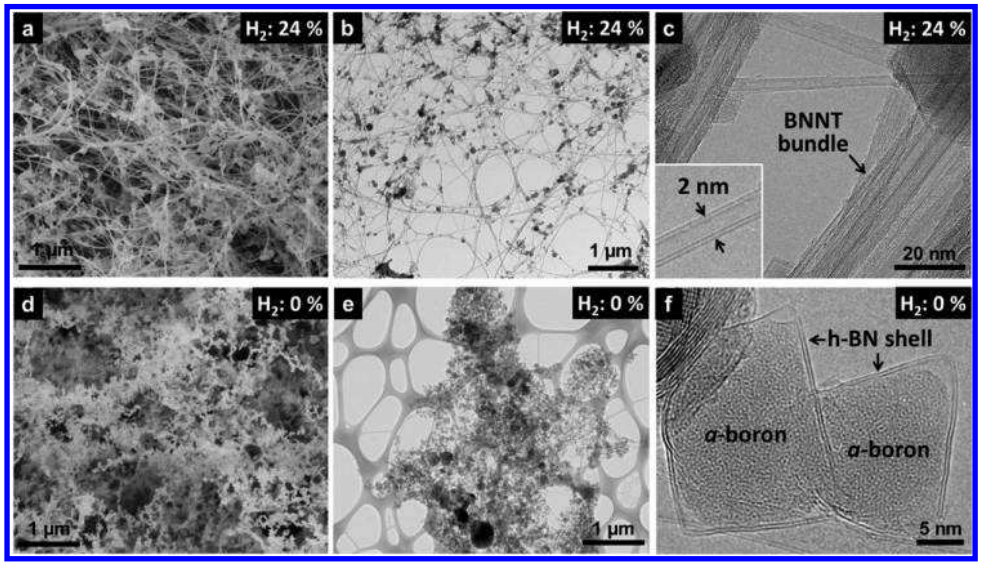

Figure 3. Effect of hydrogen on the morphological properties of reaction products in the HABS process. (a) SEM image of the sample produced with 24 vol % H_2, showing abundant fibrous materials across the sample. (b, c) TEM images showing the tubular structure of the fibrous materials observed in the SEM image in (a). (d) SEM image of the sample produced without H_2 (0 vol %). (e, f) TEM images showing boron particulates encapsulated with hBN shells.

TEM images (Figure 3d,e) indicate that the majority of the materials are aggregated particulates rather than nanotubes. The high-magnification TEM image (Figure 3f) reveals that those particles are amorphous boron particles encapsulated with a couple of hBN layers, implying incomplete reaction between B droplets and N_2.

Thermofluid Simulation. In the HABS process, complete vaporization of the hBN feedstock followed by fast and abundant nucleation of nanosized B droplets is a prerequisite for effective BNNT growth. We investigated the effects of hydrogen on such physical processes using numerical simulation based on magnetohydrodynamic theory.[21] Vaporization of hBN feedstock by the plasma plume was considered using a particle-in-cell approach;[22,23] however, the dissociation of the vaporized feedstock and the subsequent nanoparticle formation were not taken into account because of the lack of thermodynamic and transport data for some chemical species. Three cases with different H_2 contents in the plasma gas (*i.e.*, 0, 12, and 24 vol %) were studied, and their plasma conditions are summarized in Table 1. A detailed description of the numerical method can be found in the Supporting Information and elsewhere.[24−26]

Figure 4 shows the distributions of the temperature, velocity, specific enthalpy, and thermal conductivity in the entire reactor calculated at a plate power of 45 kW (equivalent to a deposited power of 30.2 kW in the plasma assuming a coupling efficiency of 67%).[27] Addition of hydrogen altered the thermofluidic fields

Table 1. Plasma Operating Conditions Employed in the Thermofluid Simulations

case	net plasma power (kW)[a]	frequency (MHz)	flow rates (slpm)		
			carrier gas (Ar)	central gas (Ar)	sheath gas ($Ar/N_2/H_2$)
0% H_2	30.2	3.0	3	30	85/135/0
12% H_2	30.2	3.0	3	30	55/135/30
24% H_2	30.2	3.0	3	30	25/135/60

[a]The coupling efficiency of the RF power was assumed to be 67%.[27] Pressure was 93 kPa in all the cases.

DOI: 10.1021/acsnano.7b08708
ACS Nano 2018, 12, 884−893

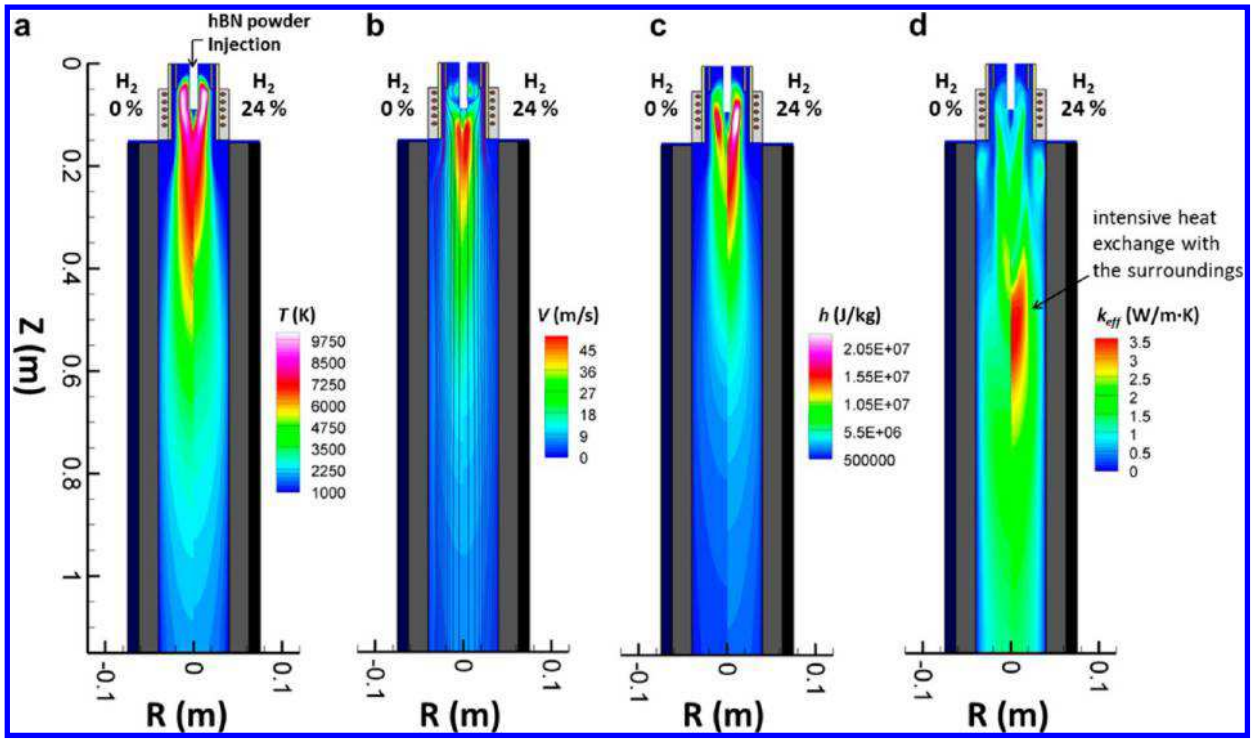

Figure 4. Thermofluidic fields calculated inside the HABS reactor: (a) temperature, (b) velocity, (c) specific enthalpy, and (d) thermal conductivity distributions calculated with 0% H_2 (left) and 24% H_2 (right). Simulation conditions: net plasma power of 30.2 kW; pressure of 93 kPa; carrier gas (Ar) at 3 L/min; central gas (Ar) at 30 L/min; sheath gas ($Ar/N_2/H_2$) at 25/135/60 (24% H_2) or 85/135/0 (0% H_2) L/min.

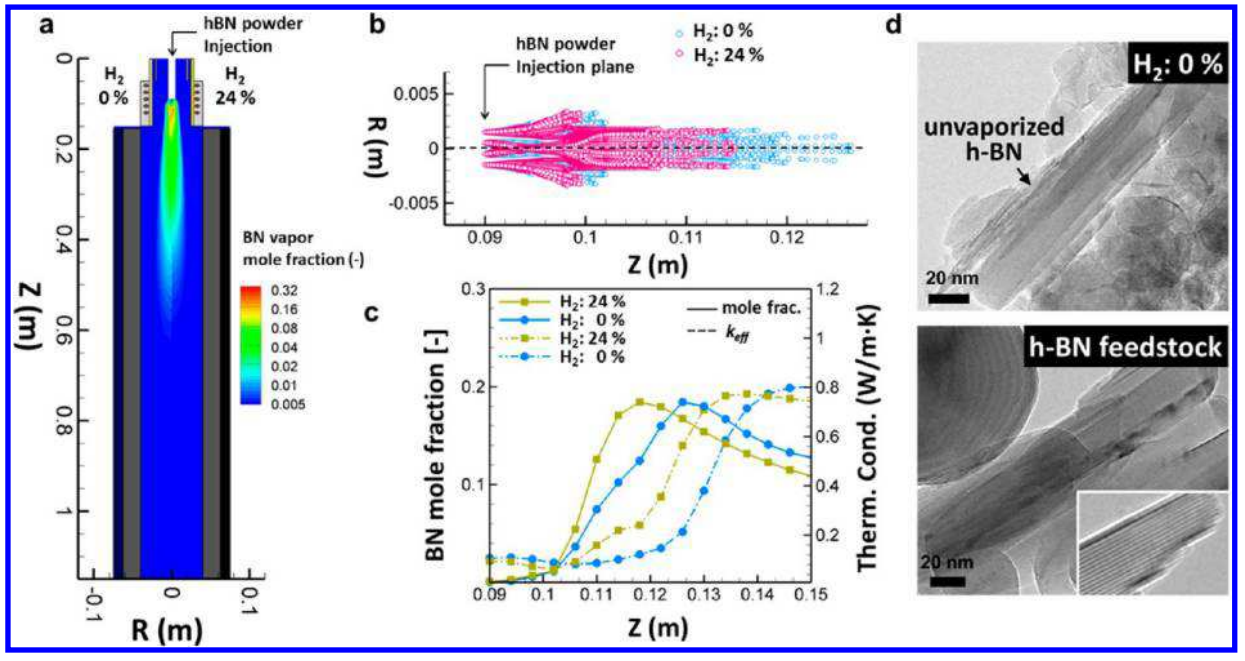

Figure 5. Effect of hydrogen on the feedstock vaporization efficiency. (a) Distribution of BN vapors calculated with 0% H_2 (left) and 24% H_2 (right). (b) Trajectories of hBN particles injected into the plasma calculated with 0% H_2 (blue) and 24% H_2 (red). (c) Axial profiles of BN vapor mole fractions (solid lines) and thermal conductivities (dot-dashed lines) calculated with 0% H_2 (blue) and 24% H_2 (green). (d) TEM image of the sample produced with 0% H_2, showing the presence of unvaporized hBN feedstock (top); TEM image of the hBN feedstock (bottom). The inset shows the layered structure of the hBN feedstock.

significantly. The most notable change is the rapid cooling of the plasma, even though its maximum temperature inside the torch was marginally elevated from 10 027 to 10 200 K, which led to a broader but shorter plasma plume. Because of its light mass, the velocity and specific enthalpy were also increased slightly. A similar trend was observed in the comparison between the cases of 12% H_2 and 24% H_2 (Figure S4). The rapid quenching of the hydrogen plasma can be explained by the improved thermal conductivity of hydrogen over the temperature range between 3500 and 4000 K; hydrogen

DOI: 10.1021/acsnano.7b08708
ACS Nano 2018, 12, 884−893

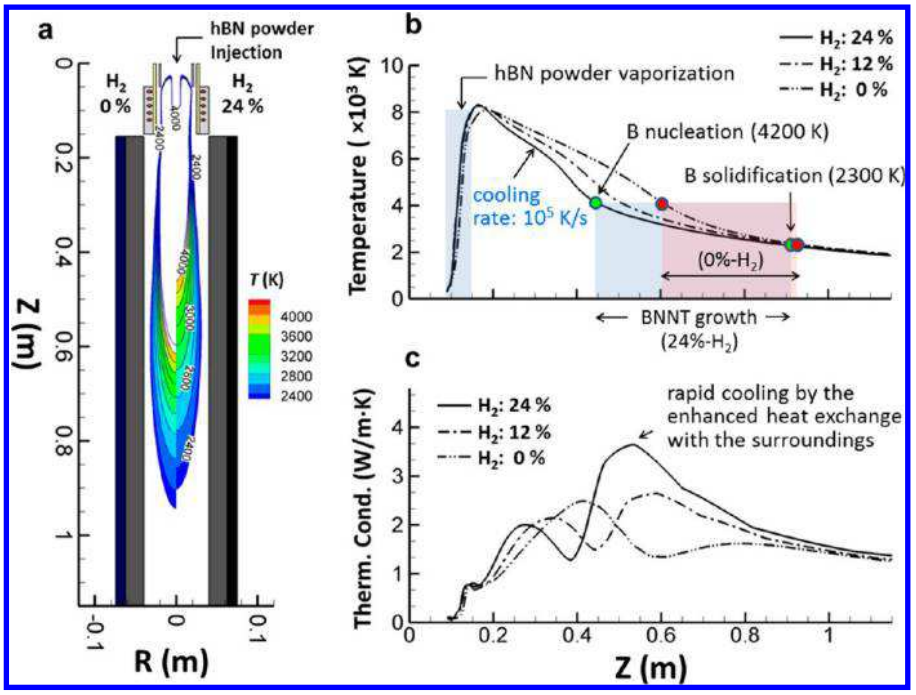

Figure 6. Effect of hydrogen on the nucleation of B droplets and the BNNT growth zones. (a) Temperature contours cut off at the B nucleation (4200 K) and solidification (2300 K) temperatures. (b) Axial temperature profiles calculated with 0% H_2, 12% H_2, and 24% H_2. The shaded areas represent the proposed BNNT growth zones for 0% H_2 (red) and 24% H_2 (blue). (c) Axial profiles of the thermal conductivities calculated with 0% H_2, 12% H_2, and 24% H_2.

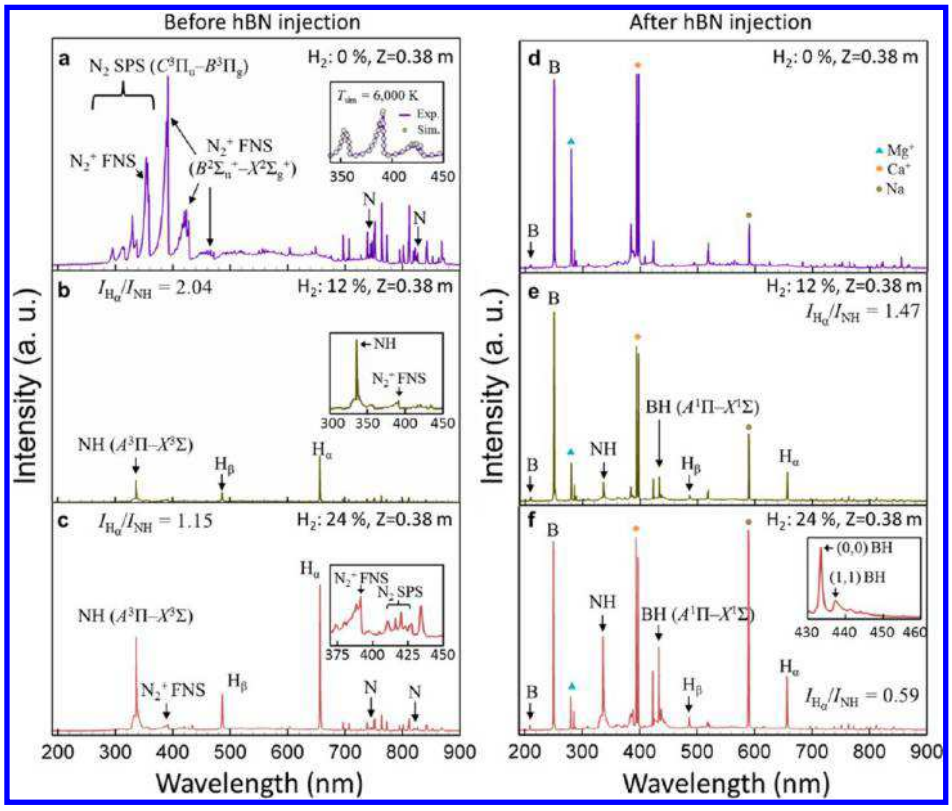

Figure 7. Optical emission spectra measured at Z = 0.38 m. (a) 0% H_2 without hBN powder injection. The inset presents a comparison between experimental and simulated spectra of the first negative system (FNS) of N_2^+ ($B^2\Sigma_u^+–X^2\Sigma_g^+$) at T = 6000 K. (b) 12% H_2 without hBN powder injection. The inset expands the NH emission band ($A^3\Pi–X^3\Sigma$) and FNS of N_2^+. (c) 24% H_2 without hBN powder injection. The inset expands the FNS of N_2^+. (d) 0% H_2 with hBN powder injection. (e) 12% H_2 with hBN powder injection. (f) 24% H_2 with hBN powder injection. The inset presents the emission bands from BH radical ($A^1\Pi–X^1\Sigma$).

DOI: 10.1021/acsnano.7b08708
ACS Nano 2018, 12, 884–893

exhibits a thermal conductivity over 50 times higher than that of nitrogen upon its dissociation at 3800 K (Figure S5).[28] Thus, hydrogen can enhance the heat exchange with the surroundings downstream, as indicated in Figure 4d, causing rapid cooling of the plasma plume. We studied how this change affects the feedstock vaporization and nucleation of B droplets.

Figure 5a shows the distributions of BN vapors produced from feedstock vaporization and compares the vaporization efficiencies of the two cases. The hBN powder was released at the tip of the injection probe at a feed rate of 1 g/min. Despite the small volume of the hot zone, BN vapors seem to form and diffuse faster in the presence of hydrogen. In Figure 5b, trajectories of the particles injected were investigated in detail. The red and blue dots represent trajectories of superparticles injected with and without hydrogen, respectively. Since the blue dots survive longer (t_v = 2.77 ms) than the red ones (t_v = 2.1 ms), hBN powder was vaporized faster in the presence of hydrogen. Given the reduced hot volume, this result is somewhat counterintuitive but may also be explained by the improved thermal conductivity of hydrogen at the hBN vaporization temperature (Figure 5c). This can accelerate heat exchange between the plasma and hBN particles. Thus, we can expect faster and more complete treatment of the feedstock in the presence of hydrogen. This simulation result is also supported by our experimental observation that unvaporized hBN feedstock was found more often with the sample produced without hydrogen, as shown in Figure 5d.

Now we investigate how hydrogen affects the nucleation of B droplets, which are assumed to serve as nucleation sites for BNNT growth. In Figure 6a, the temperature contours above the B nucleation temperature (4200 K) and below the B solidification temperature (2300 K) were cut off.[29] In this zone, B particles are in the molten phase and thus active for BNNT nucleation and growth. With hydrogen this active zone appeared earlier because of the faster cooling of the plasma jet. The axial temperature profiles for both cases are plotted in Figure 6b. In the presence of hydrogen, a steep temperature gradient with a high cooling rate (10^5 K/s) is established between Z = 0.2 m and Z = 0.4 m as a result of the enhanced thermal conductivity at the axial position between Z = 0.4 m and Z = 0.7 m, as indicated in Figure 6c. Such quenching of the reaction stream gives rise to supersaturation of the B vapors and their rapid condensation into nanosized B droplets through homogeneous nucleation.[30] However, in the absence of hydrogen, a gradual cooling rate (10^4 K/s) is observed, which significantly delays the nucleation of B droplets and consequently reduces the BNNT growth time. Once B droplets are formed, it is also important to maintain the temperature above the B solidification limit (~2300 K) in order to extend the BNNT growth. Hydrogen is also found to extend the active zone toward downstream because of the latent heat released upon recombination of H atoms starting at 3800 K. In Figure 6b, the effective BNNT growth zones are marked with shaded areas for each case, and an extended BNNT growth zone with hydrogen can be clearly seen.

Optical Emission Spectroscopy. To investigate the chemical species generated and their spatial evolution along the reactor axis, optical emissions were measured at three different axial positions: Z = 0.38, 0.48, and 0.88 m from the top of the plasma torch. Figure 7a shows a spectrum measured at Z = 0.38 m in the absence of hydrogen before hBN injection. The measured spectrum represents a typical nitrogen plasma, the most prominent lines being the second positive system of N_2 ($C^3\Pi_u$–$B^3\Pi_g$, (0,0), (1,2), (0,1), (1,3), and (0,2) bands at 333.7, 353.6, 357.6, 375.5, and 380.3 nm) and the first negative system of N_2^+ ($B^2\Sigma_u^+$–$X^2\Sigma_g^+$, (3,1), (1,1), (0,0), (1,2), (0,1), and (0,2) bands at 329.8, 388.4, 391.4, 423.6, 427.8, and 470.9 nm).[31] The unassigned peaks in the range of 700–900 nm are mostly from atomic Ar lines (Figure S6). Comparison with a synthetic spectrum[32] indicated a plasma temperature of around 6000 K (inset of Figure 7a; also see Figure S7 for the details), which is slightly lower than that for the complete dissociation of N_2 molecules (>7000 K).[28] Although atomic N lines were observed at 742–747 and 818–872 nm,[33] their intensities are weak, suggesting that most of the N radicals freed from the dissociation of N_2 sheath gas might have recombined into N_2 molecules or N_2^+ ions upon entering the reactor zone, where the plasma cooled below the N_2 dissociation limit. Thus, in the absence of hydrogen, the major N-containing species detected in the reactor zone are relatively inert N_2 molecules and N_2^+ ions rather than N radicals.

In the presence of hydrogen, several species were newly observed (Figure 7b,c). The Balmer lines of atomic H (*e.g.*, H_α, H_β, and H_γ at 656.2, 486.1, and 434.0 nm)[33] were clearly identified, while the H_2 molecular band (*i.e.*, the Fulcher-α band at 590–640 nm)[34] was relatively weak, suggesting effective dissociation of H_2 into H atoms. An equilibrium composition calculation for a hydrogen plasma shows the maximum density of H at about 3800 K.[28] The presence of H radicals notably altered the emission lines from N-containing species: the emissions from excited N_2 and N_2^+ species were significantly suppressed, while NH molecular emission lines (*i.e.*, $A^3\Pi$–$X^3\Sigma$, (0,0) and (1,1) bands at 336.0 and 337.0 nm)[31] newly appeared and became most prominent among N-containing species. Formation of N_2 molecules and N_2^+ ions from N radicals might have been suppressed by H radicals *via* NH formation; however, the formation of other N–H-containing species such as NH_2 or NH_3 (Schuster's emission band around 564 nm)[31] were not detected at this position because of the high temperature. The NH free radical is known to be a good BN precursor in the synthesis of BNNTs.

With hBN injection, more emission lines were observed. Figure 7d shows a spectrum obtained without hydrogen. First, atomic B emission lines were detected at 206.7, 208.9, and 249.7 nm, suggesting dissociation of vaporized hBN powder into atomic B and N.[33] Other new emission lines were primarily due to impurities (*e.g.*, Mg^+, Ca^+, and Na) present in the hBN feedstock.[33] In the presence of hydrogen (Figure 7e,f), new emission bands from the BH radical ($A^1\Pi$–$X^1\Sigma$, (0,0) and (1,1) bands at 433.1 nm and 436.7)[31] were also observed with the NH emission bands. The ratio of H_α and NH band intensities (I_{H_α}/I_{NH}) decreased after hBN injection, indicating additional consumption of H radicals through BH formation. In Figure 7e,f, the spectra were normalized to the intensity of the atomic B line at 249.7 nm and clearly show that the relative intensities of both the NH and BH bands increased as the hydrogen content in the plasma gas increased from 12 to 24 vol %. Thus, the presence of hydrogen promotes the formation of BH and NH radicals, which could be excellent B or N sources for B droplets, facilitating the continuous growth of BNNTs.

The reactivity of BH and NH radicals and N_2 with a B cluster (*i.e.*, B_{13}, a BNNT seed) was investigated using density functional theory (DFT). (Unlike their carbon analogues, predicting stable structures of boron clusters is intricate because of the electron deficiency of elemental boron.[35,36] For our

DOI: 10.1021/acsnano.7b08708
ACS Nano 2018, 12, 884–893

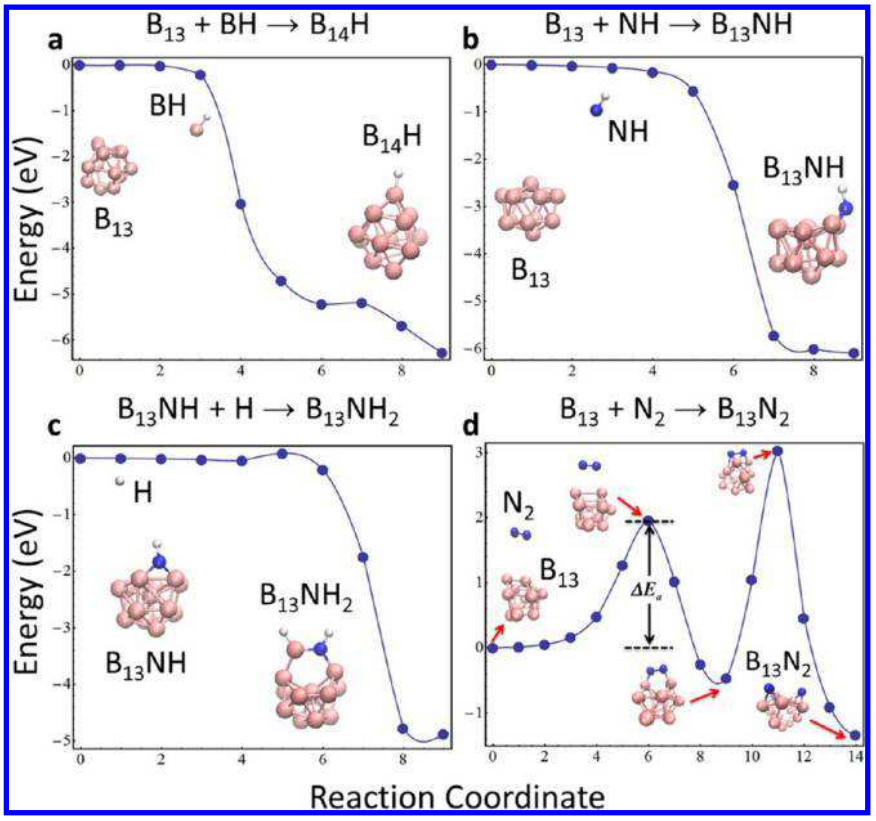

Figure 8. DFT-calculated reaction coordinate diagrams: (a) B_{13} + BH radical; (b) B_{13} + NH radical; (c) $B_{13}NH$ + H radical; (d) B_{13} + N_2 molecule.

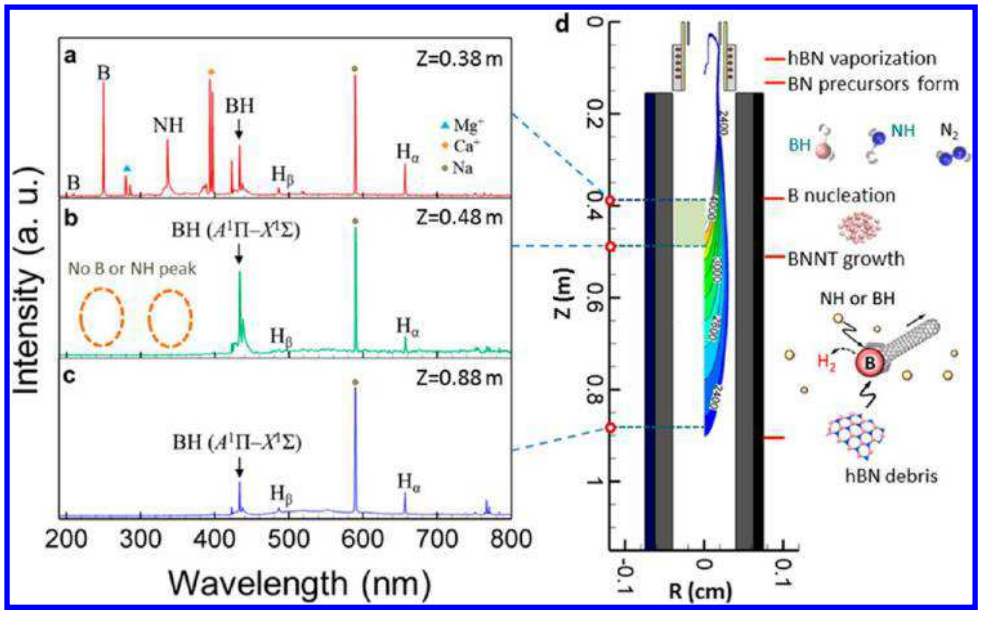

Figure 9. Spatial evolution of chemical species (24% H_2) and a BNNT growth mechanism proposed for the HABS process. (a–c) Spectra measured at (a) Z = 0.38 m, (b) Z = 0.48 m, and (c) Z = 0.88 m. (d) Proposed BNNT growth mechanism for the HABS process.

current study, we chose a B_{13} cluster as it allowed us to explore different coordination modes of boron at relatively low computational cost (Figure S10); for other clusters such as B_{12}, see Figure S11). The transition states for their reaction pathways upon binding were obtained by the nudged elastic band (NEB) method (Figure 8).[37−41] The results showed that binding of BH and NH radicals to a B cluster is highly favorable energetically, with binding energies (E_b) of −6.28 and −6.09 eV, respectively. Moreover, the profile of the total energy of each intermediate image exhibited no activation energy barrier (ΔE_a) in both cases. However, the reaction of a N_2 molecule with a B cluster showed a distinctively different pathway with two high energy barriers. As indicated in Figure 8d, the first energy barrier (ΔE_a = 1.96 eV) is associated with the formation of a B_{13}−N_2 compound, followed by the second energy barrier (ΔE_a = 3.50 eV) due to the N_2 bond dissociation. Compared

DOI: 10.1021/acsnano.7b08708
ACS Nano 2018, 12, 884−893

with the substantial activation barriers for N_2 adsorption to the B cluster, the zero activation barriers upon reaction of BH and NH free radicals indicates their relatively fast reaction toward B clusters, which promotes faster growth of BNNTs. We also calculated the subsequent reaction of a $B_{13}NH$ compound with a H radical. The result predicted sp^2 hybridization of the BN precursor as shown in Figure 8c. A low-barrier reaction pathway (ΔE_a = 0.08 eV) was also observed, indicating that this reaction is fast and thermodynamically favored.

A recent theoretical study showed that BN radical could also be an effective and direct BN source for BNNT growth.[42] We observed a trace of the BN triplet system ($A^3\Pi-X^3\Pi$, (0,0), (1,1), (0,1), and (1,2) bands at 359.9, 362.5, 380.3, and 382.9),[31,43] but its intensity was much weaker than those of BH or NH radicals (see Figures 7d–f and S8), implying that regeneration of BN radicals from the dissociated feedstock is not favorable in the HABS process. Thus, BN radicals would not be the main BNNT precursors in our plasma process. The spatial evolution of the chemical species along the reactor axis is presented in Figure 9. B and NH radicals disappeared relatively fast, while BH and H radicals survived longer (Figure 9c). This is probably due to the nucleation of B droplets (Figure 9b) and their reaction with NH radicals to form BNNTs or hBN nanodebris[42] rather than because they have shorter lifetimes (B, 3.8 ± 0.2 ns;[44] NH, 347 ± 5 ns[45]) compared with BH (125 ± 5 ns)[46] and H (12.5 ns)[47] radicals; however it must be emphasized that OES measures only excited species whose populations are affected not only by the number density of ground-state species but also by other parameters such as the excitation cross section, electron density, and electron temperature.

On the basis of the observations so far, a BNNT growth mechanism in the HABS process is proposed in Figure 9d. Initially, B, N, and H radicals are generated from the dissociation of the feedstock mixture by the high-temperature plasma (>7000 K). From those vapors, BN precursors such as BH and NH radicals are formed as the temperature decreases (5000–6000 K). In the absence of hydrogen, most of the N radicals freed from the feedstock mixture recombine into relatively inert N_2 or N_2^+, and consequently, the BNNT growth is greatly limited by the slow reaction between B droplets and N_2. However, in the presence of hydrogen, H radicals stabilize B and N radicals as BH and NH radicals, which are effective precursors for BNNT growth, as demonstrated by our DFT calculations. As the temperature decreases further (<4200 K), B droplets are formed and become available for BNNT nucleation and growth. The nucleation may occur in the shaded area in Figure 9d where the atomic B lines disappeared (Figure 9b), which is in line with the numerical simulation result. Finally, by incorporating NH and BH radicals or hBN nanodebris, BNNTs continue to grow to micron length even at atmospheric pressure.

CONCLUSIONS

Both thermofluid simulation and OES measurements were performed to understand the role of hydrogen in the rapid growth of BNNTs by high-temperature plasma. This study found that the presence of hydrogen affects both physical and chemical processes favorable to the BNNT growth. First, hydrogen enhances vaporization of the feedstock by improving the heat transfer rate at the hBN vaporization temperature (~3200 K), which leads to faster and more complete treatment of the feedstock. At the reactor downstream, the high heat transfer rate also accelerates the heat exchange with the surroundings, causing rapid quenching of the reaction stream. This results in the supersaturation of B vapors and gives rise to the abundant formation of nanosized B droplets accessible for BNNT nucleation and growth. Hydrogen is also found to extend the active BNNT growth zone toward the reactor downstream by maintaining the gas temperature above the B solidification limit (~2300 K) through release of the recombination heat of H atoms, which starts at 3800 K. The OES measurements revealed that the presence of hydrogen also promotes the formation of BH and NH radicals in the early stage of the process while suppressing the recombination of the freed N radicals into N_2 or N_2^+. DFT calculations showed that those radicals can be effective BN sources through their interactions with B droplets. These findings will provide important insights into further process optimization and development of new BNNT synthesis methods.

METHODS

BNNT Synthesis and Characterization. BNNTs were synthesized by the hydrogen-assisted BNNT synthesis (HABS) method as described elsewhere.[19] A commercial induction plasma torch (Tekna PS-50, Tekna Systems, Inc.) composed of a five-turn coil and a ceramic tube with an internal diameter of 50 mm was employed for the stable plasma generation.[48] The torch was operated with radio-frequency (RF) power at a frequency of ~3.0 MHz (Lepel Co.). The synthesis experiments were preceded by a 1 h reactor preheating cycle and lasted for 4 h. The reaction products were collected from the collection chamber and characterized without further postprocessing.

The morphological properties of the samples were analyzed by SEM (Hitachi, S4700) and TEM (FEI Titan cubed 80-300). The SEM samples were prepared directly from the as-produced samples without any further treatment. Each sample was imaged with a 2 kV, 5 μA probe current at a working distance of 8 mm. TEM samples were prepared by dispersing few milligrams of the as-produced samples in deionized water using bath sonication for 10 min. The solutions were deposited on lacy carbon TEM grids, and images were acquired at 300 kV.

Thermofluid Simulations. The thermofluidic fields inside the reactor were calculated using magnetohydrodynamic theory, involving conservation equations for mass, momentum, and energy coupled with Maxwell's equations (*e.g.*, the magnetic vector potential equation).[21] Turbulence was considered using the $K-\varepsilon$ turbulence model. Local thermodynamic equilibrium was assumed for the calculation of thermodynamic and transport properties of plasma gases (*e.g.*, density, specific heat at constant pressure, viscosity, thermal conductivity, electrical conductivity, and radiation losses).[28] The injection and vaporization of hBN feedstock was also taken into account by a particle-in-cell approach,[22,23] but chemical reactions that lead to the formation of BN precursors and nucleation of BNNTs were not considered because of the complexity and total lack of thermodynamic, transport, and reaction data for some B–N–H-containing species at high temperatures (1000–10000 K). Lastly, a two-dimensional axially symmetric computational domain was employed. More details on the governing equations, computational domain, and boundary conditions can be found in the Supporting Information or elsewhere.[24−26]

Optical Emission Spectroscopy. The optical emission spectra were recorded with a modular spectrometer (JAZ-EL200-XR1, Ocean Optics, with 1.7 nm fwhm resolution) over the wavelength range from 200 to 1025 nm. The emission light was collected through holes in the graphite liner and transported to the spectrometer by an optical fiber (QMMJ-55-UVVIS-200/240-2PCBL-0.25, OZ Optics Ltd., with a core size of 200 μm). To estimate the plasma temperature, spectra of the first negative system of N_2^+ ($B^2\Sigma_u^+-X^2\Sigma_g^+$) were synthesized for given temperatures using the LIFBASE 2.1.1 software (SRI International)[32] and compared with a spectrum obtained experimentally.

DFT Calculations. We carried out the DFT calculations using the generalized gradient approximation (GGA) with the Perdew–Burke–

DOI: 10.1021/acsnano.7b08708
ACS Nano 2018, 12, 884–893

Ernzehof (PBE) exchange−correlation functional as implemented in the Vienna *Ab Initio* Simulation Package (VASP). The basis set consisted of plane waves with a cutoff energy of 600 eV, and the projector-augmented wave (PAW) method with the frozen core approximation was used. The dimensions of the supercell were 30 Å × 30 Å × 30 Å to avoid the interactions between periodic images. The integration over the Brillouin zone was performed using the Monkhorst−Pack method with a 1 × 1 × 1 *k*-point grid. The optimized configurations of the initial and final states were obtained by relaxing all of the atomic coordinates using the conjugate-gradient algorithm until the residual force became less than 0.01 eV/Å. The transition states for the reaction pathway were obtained by using the climbing-image NEB method. The total number of intermediate images was set to eight, except for the case of N_2 adsorption, in which eight and four intermediate images were used for the first and second energy barriers, respectively.

ASSOCIATED CONTENT

Supporting Information

The Supporting Information is available free of charge on the ACS Publications website at DOI: 10.1021/acsnano.7b08708.

SEM images of the sample produced with 12% H_2 (Figure S1); governing equations, computational domain (Figure S2), boundary conditions (Figure S3 and Table S1), and hBN particle injection conditions (Table S2) for the thermofluid simulation; comparison of thermofluidic fields calculated with 12% H_2 and 24% H_2 (Figure S4); comparison of thermal conductivities of gases (Figure S5); emission spectrum obtained with the blank environment (Figure S6); estimation of the plasma temperature (Figure S7); BN emission spectrum (Figure S8); DFT calculations with different initial configurations of B_{13} cluster (Figure S9); profiles of the total energies upon binding of BH and NH radicals to B_{13} clusters with different boron coordination numbers (Figure S10); DFT calculations on reactions between B_{12} cluster and various radicals (Figure S11) (PDF)

AUTHOR INFORMATION

Corresponding Authors

*E-mail: KeunSu.Kim@nrc-cnrc.gc.ca.
*E-mail: Benoit.Simard@nrc-cnrc.gc.ca.

ORCID

Keun Su Kim: 0000-0001-7159-5978

Notes

The authors declare no competing financial interest.

ACKNOWLEDGMENTS

The authors thank G. Chan for SEM analysis and acknowledge support from the NRC-Security Materials Technology Program.

REFERENCES

(1) Hata, K.; Futaba, D. N.; Mizuno, K.; Namai, T.; Yumura, M.; Iijima, S. Water-assisted Highly Efficient Synthesis of Impurity-free Single-walled Carbon Nanotubes. *Science* **2004**, *306*, 1362−1364.

(2) Blase, X.; Rubio, A.; Louie, G.; Cohen, M. L. Stability and Band Gap Constancy of Boron Nitride Nanotubes. *Europhys. Lett.* **1994**, *28*, 335−340.

(3) Arenal, R.; Blase, X.; Loiseau, A. Boron-Nitride and Boron-Carbonitride Nanotubes: Synthesis, Characterization and Theory. *Adv. Phys.* **2010**, *59*, 101−179.

(4) Kim, K. S.; Jakubinek, M. B.; Martinez-Rubi, Y.; Ashrafi, B.; Guan, J.; O'Neill, K.; Plunkett, M.; Hrdina, A.; Lin, S.; Denommee, S.; Kingston, C. T.; Simard, B. Polymer Nanocomposites from Free-standing Macroscopic Boron Nitride Nanotubes Assemblies. *RSC Adv.* **2015**, *5*, 41186−41192.

(5) Kang, J. H.; Sauti, G.; Park, C.; Yamakov, V. I.; Wise, K. E.; Lowther, S. E.; Fay, C. C.; Thibeault, S. A.; Bryant, R. G. Multifunctional electroactive nanocomposites based on piezoelectric boron nitride nanotubes. *ACS Nano* **2015**, *9*, 11942−11950.

(6) Chopra, N. G.; Luyken, R. J.; Cherrey, K.; Crespi, V. H.; Cohen, M. L.; Louie, S. G.; Zettl, A. *Science* **1995**, *269*, 966−967.

(7) Golberg, D.; Bando, Y.; Tang, C. C.; Zhi, C. Y. Boron Nitride Nanotubes. *Adv. Mater.* **2007**, *19*, 2413−2432.

(8) Rao, C. N. R.; Govindaraj, A. Synthesis of Inorganic Nanotubes. *Adv. Mater.* **2009**, *21*, 4208−4233.

(9) Zhi, C. Y.; Bando, Y.; Tang, C. C.; Golberg, D. Boron Nitride Nanotubes. *Mater. Sci. Eng., R* **2010**, *70*, 92−111.

(10) Golberg, D.; Bando, Y.; Huang, Y.; Terao, T.; Mitome, M.; Tang, C.; Zhi, C. Boron Nitride Nanotubes and Nanosheets. *ACS Nano* **2010**, *4*, 2979−2993.

(11) Kim, K. S.; Kim, M. J.; Park, C.; Fay, C. C.; Chu, S.-H.; Kingston, C. T.; Simard, B. Scalable Manufacturing of Boron Nitride Nanotubes and Their Assemblies: A Review. *Semicond. Sci. Technol.* **2017**, *32*, 013003.

(12) Golberg, D.; Bando, Y.; Eremets, M.; Takemura, K.; Kurashima, K.; Yusa, H. Nanotubes in Boron Nitride Laser Heated at High Pressure. *Appl. Phys. Lett.* **1996**, *69*, 2045−2047.

(13) Lee, R. S.; Gavillet, J.; Lamy de la Chapelle, M.; Loiseau, A.; Cochon, J.-L.; Pigache, D.; Thibault, J.; Willaime, F. Catalyst-free Synthesis of Boron Nitride Single-wall Nanotubes with a Preferred Zig-zag Configuration. *Phys. Rev. B: Condens. Matter Mater. Phys.* **2001**, *64*, 121405.

(14) Shimizu, Y.; Moriyoshi, Y.; Tanaka, H.; Komatsu, S. Boron nitride nanotubes, webs, and coexisting amorphous phase formed by the plasma jet method. *Appl. Phys. Lett.* **1999**, *75*, 929−931.

(15) Lee, C. M.; Choi, S. I.; Choi, S. S.; Hong, S. H. Synthesis of Boron Nitride Nanotubes by Arc-Jet Plasma. *Curr. Appl. Phys.* **2006**, *6*, 166−170.

(16) Yoo, C. S.; Akella, J.; Cynn, H.; Nicol, M. Direct Elementary Reactions of Boron and Nitrogen at High Pressures and Temperatures. *Phys. Rev. B: Condens. Matter Mater. Phys.* **1997**, *56*, 140−146.

(17) Smith, M. W.; Jordan, K. C.; Park, C.; Kim, J.-W.; Lillehei, P. T.; Crooks, R.; Harrison, J. S. Very Long Single- and Few-Walled Boron Nitride Nanotubes *via* the Pressurized Vapor/Condenser Method. *Nanotechnology* **2009**, *20*, 505604.

(18) Fathalizadeh, A.; Pham, T.; Mickelson, W.; Zettl, A. Scaled synthesis of boron nitride nanotubes, nanoribbons, and nanococoons using direct feedstock injection into an extended-pressure, inductively-coupled thermal plasma. *Nano Lett.* **2014**, *14*, 4881−4886.

(19) Kim, K. S.; Kingston, C. T.; Hrdina, A.; Jakubinek, M. B.; Guan, J.; Plunkett, M.; Simard, B. Hydrogen-Catalyzed, Pilot-Scale Production of Small-Diameter Boron Nitride Nanotubes and Their Macroscopic Assemblies. *ACS Nano* **2014**, *8*, 6211−6220.

(20) Arenal, R.; Stephan, O.; Cochon, J. L.; Loiseau, A. Root-Growth Mechanism for Single-Walled Boron Nitride Nanotubes in Laser Vaporization Technique. *J. Am. Chem. Soc.* **2007**, *129*, 16183−16189.

(21) Gleizes, A.; Gonzalez, J. J.; Freton, P. Thermal Plasma Modelling. *J. Phys. D: Appl. Phys.* **2005**, *38*, R153−R183.

(22) Proulx, P.; Mostaghimi, J.; Boulos, M. I. Heating of Powders in an RF Inductively Coupled Plasma under Dense Loading Conditions. *Plasma Chem. Plasma Process.* **1987**, *7*, 29−52.

(23) Chen, X. Particle Heating in a Thermal Plasma. *Pure Appl. Chem.* **1988**, *60*, 651−662.

(24) Xue, S. W.; Proulx, P.; Boulos, M. I. Extended-field Electromagnetic Model for Inductively Coupled Plasma. *J. Phys. D: Appl. Phys.* **2001**, *34*, 1897−1906.

(25) Kim, K. S.; Moradian, A.; Mostaghimi, J.; Soucy, G. Modeling of Induction Plasma Process for Fullerene Synthesis: Effect of Plasma Gas Composition and Operating Pressure. *Plasma Chem. Plasma Process.* **2010**, *30*, 91−110.

DOI: 10.1021/acsnano.7b08708
ACS Nano 2018, 12, 884−893

(26) Kim, K. S.; Moradian, A.; Mostaghimi, J.; Alinejad, Y.; Shahverdi, A.; Simard, B.; Soucy, G. Synthesis of Single-Walled Carbon Nanotubes by Induction Thermal Plasma. *Nano Res.* **2009**, *2*, 800−817.
(27) Boulos, M. I. The Role of Transport Phenomena and Modeling in the Development of Thermal Plasma Technology. *Plasma Chem. Plasma Process.* **2016**, *36*, 3−28.
(28) Boulos, M. I.; Fauchais, P.; Pfender, E. *Thermal Plasmas: Fundamentals and Applications*; Plenum Press: New York, 1994; pp 385−407.
(29) Okamoto, H. B-N (Boron-Nitrogen). *J. Phase Equilib.* **2000**, *21*, 208−208.
(30) Shigeta, M.; Murphy, A. B. Thermal Plasmas for Nanofabrication. *J. Phys. D: Appl. Phys.* **2011**, *44*, 174025.
(31) Pearse, R. W. B.; Gaydon, A. G. *The Identification of Molecular Spectra*; Chapman and Hall: London, 1963.
(32) Luque, J.; Crosley, D. R. *LIFBASE: Database and Spectral Simulation*, version 1.5; SRI International Report MP 99-009; SRI International: Menlo Park, CA, 1999.
(33) NIST. Atomic Spectra Database, 2017. https://www.nist.gov/pml/atomic-spectra-database (accessed Sept 12, 2017).
(34) Fantz, U.; Heger, B. Spectroscopic Diagnostics of the Vibrational Population in the Ground State of H_2 and D_2 molecules. *Plasma Phys. Controlled Fusion* **1998**, *40*, 2023−2032.
(35) Shang, B.; Yuan, L.-F.; Zeng, X. C.; Yang, J. *Ab Initio* Prediction of Amorphous B84. *J. Phys. Chem. A* **2010**, *114*, 2245−2249.
(36) Zhai, H.-J.; Kiran, B.; Li, J.; Wang, L. − S. Hydrocarbon Analogues of Boron Clusters - Planarity, Aromaticity and Antiaromaticity. *Nat. Mater.* **2003**, *2*, 827−833.
(37) Perdew, J. P.; Burke, K.; Ernzerhof, M. Generalized Gradient Approximation Made Simple. *Phys. Rev. Lett.* **1996**, *77*, 3865−3868.
(38) Kresse, G.; Furthmüller, J. Efficient Iterative Schemes for *Ab Initio* Total-Energy Calculations Using a Plane-Wave Basis Set. *Phys. Rev. B: Condens. Matter Mater. Phys.* **1996**, *54*, 11169−11186.
(39) Jonsson, H.; Mills, G.; Jacobsen, K. W. Nudged Elastic Band Method for Finding Minimum Energy Paths of Transitions. In *Classical and Quantum Dynamics in Condensed Phase Simulations*; Berne, B. J., Ciccotti, G., Coker, D. F., Eds.; World Scientific: Singapore, 1998; pp 385−404.
(40) Henkelman, G.; Uberuaga, B. P.; Jónsson, H. A Climbing Image Nudged Elastic Band Method for Finding Saddle Points and Minimum Energy Paths. *J. Chem. Phys.* **2000**, *113*, 9901−9904.
(41) Henkelman, G.; Jónsson, H. Improved Tangent Estimate in the Nudged Elastic Band Method for Finding Minimum Energy Paths and Saddle Points. *J. Chem. Phys.* **2000**, *113*, 9978−9985.
(42) Han, L.; Krstic, P. A Path for Synthesis of Boron-nitride Nanostructures in Volume of Arc Plasma. *Nanotechnology* **2017**, *28*, 07LT01.
(43) Dutouquet, C.; Acquaviva, S.; Hermann, J. Detection of Boron Nitride Radicals by Emission Spectroscopy in a Laser-induced Plasma. *Spectrochim. Acta, Part B* **2001**, *56*, 629−635.
(44) Andersen, T.; Jessen, K. A.; Sørensen, G. Mean-life Measurements of Excited Electronic States in Neutral and Ionic Species of Beryllium and Boron. *Phys. Rev.* **1969**, *188*, 76−81.
(45) Cvejanovic, D.; Adams, A.; King, C. G. Radiative Lifetime Measurements of NH and CH using Electron-photon Delayed Coincidence Method. *J. Phys. B: At. Mol. Phys.* **1978**, *11*, 1653−1662.
(46) Dufayard, J.; Nedelec, O. Lifetime of the BH $A^1\Pi$ State Excited by a Pulsed Dye Laser. *J. Chem. Phys.* **1978**, *69*, 4708−4709.
(47) Ankudinov, V. A.; Bobashev, S. V.; Andreev, E. P. Measurement of Lifetimes of Excited States of the Hydrogen Atom. *Sov. Phys. JETP* **1965**, *21*, 26−32.
(48) Boulos, M. I. The Inductively Coupled R.F. (radio frequency) Plasma. *Pure Appl. Chem.* **1985**, *57*, 1321−1352.

DOI: 10.1021/acsnano.7b08708
ACS Nano 2018, 12, 884−893